Preponderant influence of disordered *P4bm* phase on the piezoelectricity of critical compositions of Na$_{0.5}$Bi$_{0.5}$TiO$_3$-based ferroelectrics

Gobinda Das Adhikary,[1] Deepak Sharma [ORCID],[1] Pooja Punetha,[1] Gudeta Jafo,[1] Getaw Abebe,[1] Anupam Mishra [ORCID],[1]
Anatoliy Senyshyn,[2] and Rajeev Ranjan [ORCID][1,*]

[1]*Department of Materials Engineering, Indian Institute of Science, Bangalore-560012, India*

[2]*Forschungsneutronenquelle Heinz Maier-Leibnitz (FRM II). Technische Universität München, Lichtenbergestrasse 1, D-85747 Garching b. München, Germany*

We investigated the phase boundaries of three Na$_{0.5}$Bi$_{0.5}$TiO$_3$-(NBT) based piezoelectric systems NBT-BaTiO$_3$ (NBT-BT), NBT-K$_{0.5}$Bi$_{0.5}$TiO$_3$ (NBT-KBT) and NBT-SrTiO$_3$ (NBT-ST), all exhibiting similar piezoelectric responses ($d_{33} \sim 180$ *pC/N*). We found that, apart from a qualitative difference (NBT-KBT/NBT-BT exhibits *R3c-P4mm* interferroelectric instability and NBT-ST does not), the critical compositions of all the three systems exhibit onset of a *disordered P4bm* phase. Our study suggests that the preponderant effect of this distortion overrides the interferroelectric instability, limiting the piezoelectric response of NBT-BT/NBT-KBT like that in NBT-ST.

I. INTRODUCTION

Among the different phenomena exhibited by ferroelectric materials, the electromechanical properties have attracted most attention. For over six decades Pb(Zr$_x$Ti$_{1-x}$)O$_3$ (PZT)-based ferroelectric perovskites have been used commercially in wide ranging applications spanning sectors like medical diagnostics, space, defense, automobiles, etc. The framework structure of perovskite (corner linked octahedra) provides flexibility to accommodate a large variety of cations and offers great scope for property tuning. Though by symmetry considerations all ferroelectrics are expected to show piezoelectricity, the discovery of a remarkable increase of piezoelectric response at the morphotropic phase boundary (MPB) of PZT [1,2] has guided subsequent research and developmental efforts in the field. In the composition-temperature phase diagram of ferroelectric solid solutions MPB separates two different ferroelectric phase regions (say tetragonal (*P4mm*) and rhombohedral (*R3m*) in PZT [2]). While this boundary is nearly vertical for PZT, for most other systems it is temperature dependent and is also referred to as polymorphic phase boundary (PPB). In the ubiquitous polycrystalline ferroelectric ceramics, MPB compositions are generally characterized by the coexistence of two ferroelectric phases. This feature enables efficient poling of polycrystalline ferroelectric specimens by increasing the probability of finding compatible domain variants across grain boundaries for domain switching [3]. The enhancement of piezoelectric response in MPB/PPB-based ferroelectrics is attributed to the ease of polarization rotation caused by the nearly flattened free energy profile [4,5], and increased contribution of the ferroelectric-ferroelastic domain walls [3,6–8].

Motivated by environmental concerns and legislations restricting the use of hazardous materials in industrial applications [9], the past two decade has witnessed a surge in interest in Pb-free piezoelectric materials [10–14]. Large piezoelectric responses comparable to PZT-based systems have been discovered in BaTiO$_3$ (BT) [13,11,15,16] and (K,Na)NbO$_3$ (KNN)-based lead-free ferroelectric systems [10,17–20]. Over the years, the Pb-free ferroelectric compound Na$_{0.5}$Bi$_{0.5}$TiO$_3$ (NBT) and its solid solutions have attracted considerable attention [21–31]. Among the known Pb-free alternatives, NBT-based piezoelectrics have the unique distinction of exhibiting very large high-field electrostrain (greater than 0.5%) [32–35]. The complex coupled structural-polar behavior of NBT (and its solid solutions) primarily owe its origin to the inherent local structural disorder caused by the qualitatively different nature of Na-O (ionic) and Bi-O (covalent) bonds and random distribution of Na and Bi on the same crystallographic site [29,36,37]. One peculiar aspect of this structural disorder is that it makes the global structure of NBT appear as monoclinic (*Cc*) [21,22,24], instead of rhombohedral (*R3c*) originally reported [38–40]. Poling can, however, suppress local structural disorder and stabilize rhombohedral (*R3c*) structure on the global scale [21,41]. The structural disorder inherent to the parent compound NBT pervades all its solid solutions, considerably affecting their properties [42–46]. Since NBT is a rhombohedral ferroelectric, a solid solution with tetragonal (*P4mm*) ferroelectric perovskites like PbTiO$_3$ (PT), BaTiO$_3$ (BT) and K$_{0.5}$Bi$_{0.5}$TiO$_3$ (KBT) can induce interferroelectric instability [47–51]. The critical MPB compositions of (1-*y*)NBT-*y*BT and (1-*z*)NBT-(*z*)KBT are $y \sim 0.06$ [52–54] and $z \sim 0.20$ [44,55,56], respectively, both giving maximum $d_{33} \sim 180$ pC/N [44,52,55,57]. Interestingly, a similar value d_{33} has been reported for a critical composition of another NBT-based system (1-x)Na$_{0.5}$Bi$_{0.5}$TiO$_3$-(x)SrTiO$_3$ (NBT-ST) for x ~ 0.20

---

*rajeev@iisc.ac.in

[58,59]. In analogy with NBT-BT and NBT-KBT, the high d_{33} in NBT-ST has been attributed to the MPB nature of its critical composition [58,60,61]. Unlike BT and KBT, $SrTiO_3$ exhibits cubic paraelectric phase down to 105 K [62]. Below 105 K, it transforms to tetragonal (space group $I\ 4/mcm$) structure involving antiphase ($a^0a^0c^-$) tilt of neighboring octahedra along the c axis [62]. ST is also known as quantum para-electric/incipient ferroelectric since the quantum fluctuations suppress the ferroelectric order [63]. It is anticipated that the nature of the critical composition of NBT-ST should be different from that of the other two systems.

Unlike most MPB/PPB ferroelectrics wherein the nature of the coexisting ferroelectric phases can be easily identified on the global scale by x-ray powder diffraction, the critical compositions of NBT-based ferroelectrics exhibit a cubiclike structure in unpoled specimens [44,52,55,64–68]. Although the similarity of d_{33} of the critical composition of NBT-ST with the d_{33} of the critical compositions of NBT-BT and NBT-KBT has prompted the possibility of MPB in NBT-ST [58,60,61], there is no clarity regarding the structural state of its critical composition. As stated above, since the end member ST does not exhibit ferroelectric $P4mm$ distortion, it is less likely that the MPB composition of NBT-ST would exhibit $R3c$-$P4mm$ interferroelectric instability. In this context, a careful structural examination of the critical composition of NBT-ST vis-à-vis the other two systems (NBT-BT/NBT-KBT) assumes significance for better appreciation of their piezoelectric responses. In this work we have resolved this fundamental issue. As part of this study, we demonstrate how Eu^{+3} rare-earth photoluminescence emission signal can be used as a powerful tool to ascertain the structural states of the critical compositions of these three systems on the local scale.

II. EXPERIMENTAL

A series of $(1-x)Na_{0.5}Bi_{0.5}TiO_3 - (x)SrTiO_3$ [NBT-(x)ST] compositions were synthesized using the conventional solid state reaction method. Dried powders of Na_2CO_3 (99.5%, Alfa Aesar), $SrCO_3$ (99%, Alfa Aesar), Bi_2O_3 (99%, Alfa Aesar), and TiO_2 (99.8%, Alfa Aesar) were weighed in sto-ichiometric ratios and mixed in an acetone medium using zirconia vials and balls in a planetary ball mill at 150 rpm for 12 h. Milled powders were dried, ground, and calcined at 900 °C for 3 h in covered alumina crucibles. The calcined powders were remilled at 150 rpm for 8 h. The remilled powder was dried and mixed with 5% PVA solution and pressed into pellets under uniaxial pressure of 100 MPa followed by cold isotropic pressure of 300 MPa. The pellets were sintered in covered alumina crucibles at 1150 °C for 4 h in air. Specimens of $(1-y)\ Na_{0.5}Bi_{0.5}TiO_3$-$(y)BaTiO_3$ [NBT-(y)BT] [46,52] and $(1-z)Na_{0.5}Bi_{0.5}TiO_3 - (z)K_{0.5}Bi_{0.5}TiO_3$ [NBT−(z)KBT] [44,55] were also synthesized using the same method. Property measurements were performed on pellets of average density ∼95%. The sintered pellets with diameters of 10–12 mm and thickness of 0.5 mm were painted with silver paste for electrical contact and poled by applying a dc field of 60 kV/cm for 30 min at room temperature. A weak-field piezoelectric coefficient (d_{33}) was measured using Piezotest, PM300 with applied force 0.25N and frequency 110 Hz. *Ex situ* thermal depoling measurements were performed in which

the samples were annealed at a set temperature for 10 min in a furnace, after which they were removed and the d_{33} was measured when the sample reached room temperature. Thermal depoling current measurements were performed using an Electrometer (Keithley, 6514) by heating poled pellets at 3 °C/min. Thermal depoling current shows a sharp peak at the temperature where poling induced long-range ferroelectric order vanishes completely. X-ray powder diffraction (XRPD) measurements were carried out using Rigaku Smartlab x-ray diffractometer with monochromatic Cu $K\alpha_1$ radiation. XRPD and neutron powder diffraction (NPD) measurements of the poled specimens were carried out after crushing the poled pellets gently to powder. The powder specimens were obtained after grinding the poled pellets. This approach offers texture free diffraction pattern while at the same time preserves the structural changes on the global scale caused by the poling field. The XRPD patterns of the unpoled specimens were collected after annealing the ground powder at 750 °C for 2h to remove the effect of residual stress, if any, incurred during the grinding process. High temperature XRPD data were collected on powders of poled pellets. Room temperature neutron powder diffraction (NPD) data were collected at the diffractometer SPODI at FRM-II, Germany (wavelength of 1.548 150 Å) [69]. High temperature NPD measurements were carried out on poled powders during heating. Structural analysis was performed by the Rietveld method using the FULLPROF program [70]. Raman and photoluminescence spectra were collected from poled and unpoled pellets using 532-nm laser attached with Lab-RAM HR (HORBA) spectrometer.

III. RESULTS AND DISCUSSION

Figure 1(a) compares the composition dependence of the longitudinal piezoelectric coefficient (d_{33}) of NBT-(x)ST, NBT-(y)BT and NBT-(z)KBT. The critical compositions exhibiting maximum d_{33} are x = 0.20, y = 0.06 and z = 0.20. The maximum value of d_{33} for all the three systems are nearly same ($d_{33} \sim 180\ pC/N$). We carried out structural analysis at close composition intervals near the critical compositions of these three systems. Consistent with previous studies, x-ray diffraction (XRD) suggests that the unpoled specimens of the critical compositions exhibit cubiclike average structure [59,52,44,64], Fig. 2(a). To understand structural differences, if any, on the local scale, we used the Eu^{+3} photoluminescence (PL) emission signal as a technique [71–73]. In brief, because of shielding from the outer $5s^2\ 5p^6$ orbitals, the discrete energy levels of the $4f^n$ valence electrons of the trivalent lanthanides are determined primarily by interactions within the lanthanide ion. In a ligand/crystal-field environment, the otherwise parity forbidden intra f-f transitions becomes possible. The PL emissions resulting from such transitions are sensitive to the local structure around the rare-earth (here Eu^{+3}). This aspect can be exploited to probe structures of materials on the local scale by doping them with rare-earth ions [74–80]. Here we have used it to unravel the nature of ferroelectric order on the local scale in the critical compositions of the three NBT-based systems: NBT-ST, NBT-BT and NBT-KBT. For the PL study, we doped the critical compositions of the three systems with very dilute Eu^{+3} concentration. The corresponding specimens were synthesized such that a small fraction of Bi^{+3} was
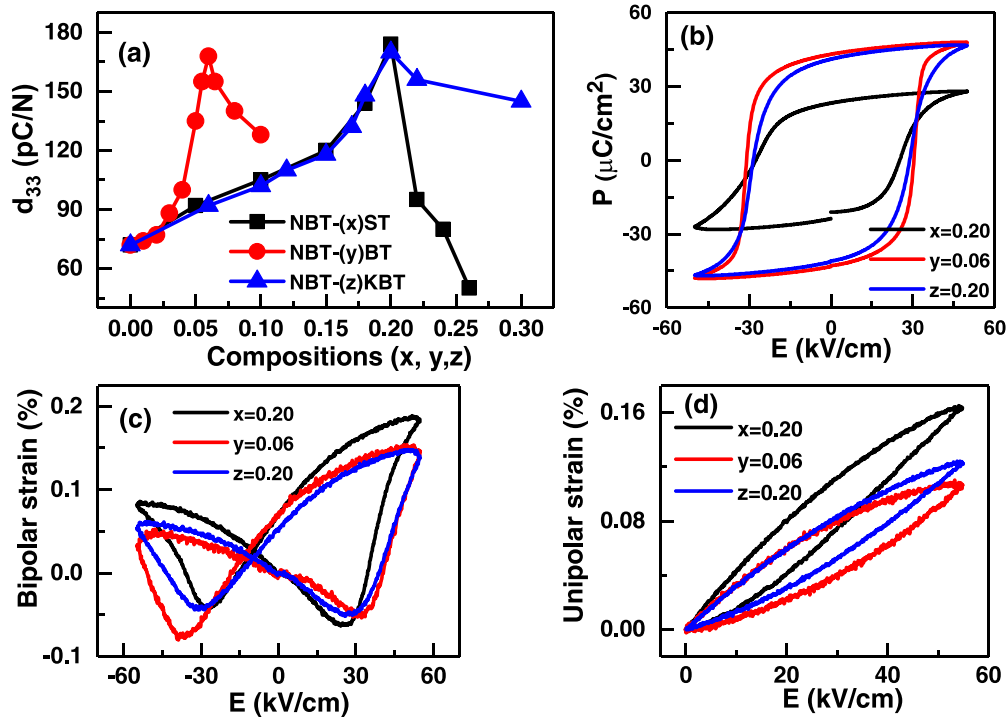
FIG. 1. (a) Composition dependence of weak-field piezoelectric coefficient (d_{33}) of (1-x)NBT-(x)ST, (1-y)NBT-(y)BT and (1-z)NBT-(z)KBT. Electric field dependence of (b) polarization, (c) bipolar strain, and (d) unipolar strain of $x = 0.20$, $y = 0.06$, and $z = 0.20$.

replaced by Eu^{+3} in the NBT part of the solid solution as per the nominal formula $Na_{0.5}Bi_{0.495}Eu_{0.005}TiO_3$. While the dilute concentration of Eu^{+3} did not affect the structural, ferroelectric, and piezoelectric properties significantly vis-à-vis their Eu^{+3} free counterparts, this small Eu^{+3} concentration is sufficient to give good PL signal to study the structural

state of these systems on the local scale [55,74,78–80], Fig. S1 and Fig. S2 in the Supplemental Material [81]. The Eu^{+3} stark bands in the different wavelength ranges in the PL spectrum correspond to $^5D_0 \rightarrow {}^7F_0$ (570–585 nm), $^5D_0 \rightarrow {}^7F_1$ (585–600 nm), $^5D_0 \rightarrow {}^7F_2$ (610–630 nm), $^5D_0 \rightarrow {}^7F_3$ (640–660 nm), and $^5D_0 \rightarrow {}^7F_4$ (680–710 nm),
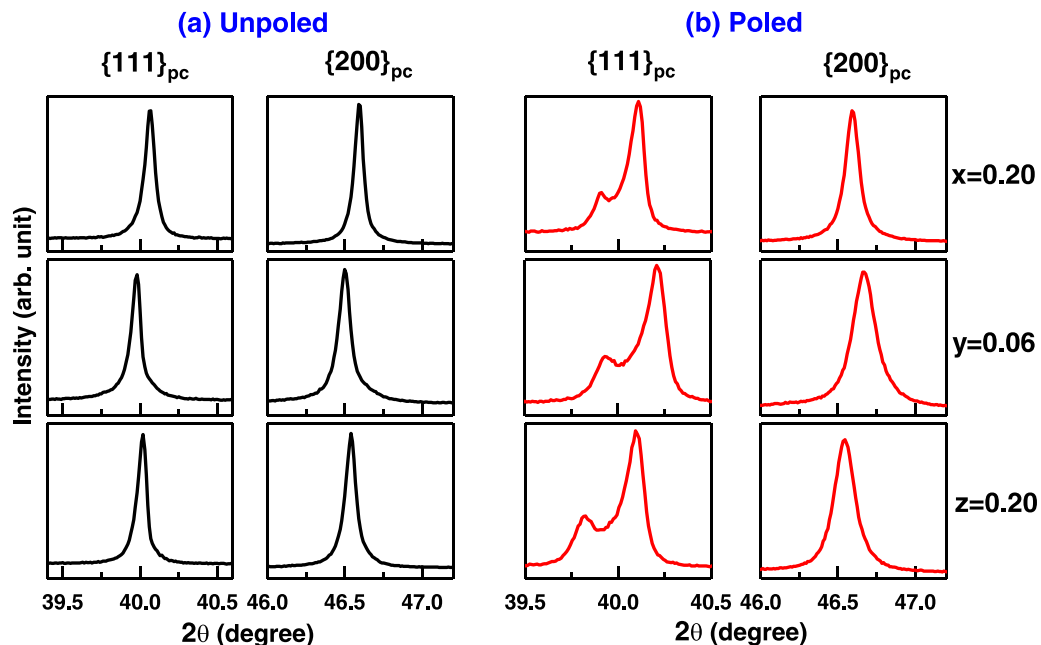

FIG. 2. X-ray powder-diffraction profiles of pseudocubic $\{111\}_{pc}$, and $\{200\}_{pc}$ of the critical compositions of NBT-xST($x = 0.20$), NBT-yBT ($y = 0.06$) and NBT-zKBT ($z = 0.20$) in (a) unpoled and (b) poled specimens.
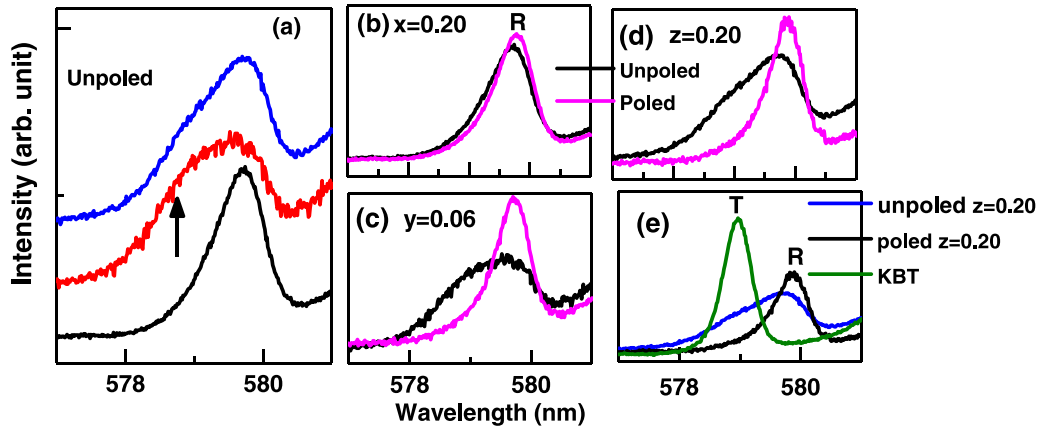
FIG. 3. (a) Comparison of the $^5D_0 \rightarrow ^7F_0$ (570-585 nm) Stark profiles in the PL spectra of Eu-doped unpoled specimens of NBT-xST (x = 0.20), NBT-yBT (y = 0.06) and NBT-zKBT (z = 0.20). In contrast to the PL spectrum of x = 0.20 which possesses one stark line in the band, y = 0.06 and z = 0.20 exhibit two Stark lines. (b–d) show the $^7F_0$ Stark profiles of the critical compositions of unpoled and poled specimens of the three systems. (e) The Stark profiles of KBT (tetragonal, *P4mm*) denoted by *T* along with profiles of poled and unpoled z = 0.20. *R* denotes the Stark profile of the *R3c* phase.

electronic transitions [72]. Since the multiplicity of the ^7F_J level increases with increasing *J*, the corresponding Stark band shows overlap of several peaks for transitions involving higher *J* values. This can hamper inferring crucial structural information in structurally heterogeneous systems (e.g., MPB/PPB), in an unambiguous manner. In contrast, the Stark band corresponding to the *J* = 0 level is expected to be a singlet. Allowing for the possibility that the position of the $^7F_0$ stark band can be slightly different for the different phases, a careful analysis of this Stark band can help in unambiguous assertion of phase coexistence, if any, on the local scale. As shown below, this strategy turned out to be successful in identifying the polar phase(s) in critical compositions of these complex ferroelectric systems.

Figure 3(a) shows a comparison of the $^7F_0$ Stark bands of the three critical compositions (NBT-xST with x = 0.20, NBT-yBT with y = 0.06 and NBT-zKBT with z = 0.20) in their unpoled state. The $^7F_0$ Stark band of the NBT-ST x = 0.20 is a singlet with peak at 579.71 nm. The $^7F_0$ Stark band of NBT-BT and NBT-KBT, on the other hand, is a doublet [Fig. 3(a)]. We also collected the PL spectrum of NBT-ST (x = 0.20) and NBT-KBT (z = 0.20) after poling. While no significant change is noticeable in the profile of poled NBT-0.20ST [Fig. 3(b)], the doublet $^7F_0$ Stark band of NBT-0.06BT [Fig. 3(c)] and NBT-0.20KBT [Fig. 3(d)] transformed to a singlet after poling. XRD measurements suggests that poling transforms the cubiclike phase to rhombohedral for all the three cases, Fig. 2(b). A comparison of the PL spectrum of unpoled NBT-0.20KBT and the PL spectrum of Eu-modified KBT (tetragonal, *P4mm* structure) reveal that the additional PL peak at ∼ 578.93 nm which vanished after poling corresponds to the tetragonal ferroelectric (*P4mm*) phase. Our PL study unambiguously confirms that the cubic like phase of NBT-KBT and NBT-BT correspond to an assemblage of tetragonal (*P4mm*) and rhombohedral (*R3c*) phases on the local scale. In contrast, the cubic like phase of NBT-ST exhibit only rhombohedral phase on the local scale. This distinctly different structural behavior of the critical compositions of

NBT-ST, NBT-BT and NBT-KBT is also manifested in the way the A_1 (TO1) Raman modes of the three systems vary with composition, Fig. S3b [81]. The sharp decrease of the frequency of this mode as the critical composition approached is NBT-BT and NBT-KBT is in consistent with the *R3c-P4mm* interferroelectric lattice instability present in both the systems. In contrast, the A_1 (TO1) mode softens gradually with composition, indicating lack of a lattice instability on approaching the critical composition in the NBT-ST system, Fig. S3b [81].

Figures S4 and S5 show the XRD patterns of the three systems above their respective critical compositions in their poled state [81]. While poled NBT-BT and NBT-KBT show the cubiclike phase transform to tetragonal (*P4mm*) [44,52,82], we could not find any signature of tetragonal *P4mm* distortion in poled NBT-ST for x > 0.20, Fig. S5 [81]. In fact, Rietveld analysis revealed that the diffraction pattern of poled NBT-ST can be fitted satisfactorily with *R3c* + cubic structural model (Fig. S6 [81]), with cubic fraction increasing with increasing ST concentration, Fig. S7a [81]. This difference in the structural states of poled NBT-BT/NBT-KBT and poled NBT-ST above their respective critical composition is also manifest in the composition dependence of their d_{33}, Fig. 1(a); the piezoelectric coefficient (d_{33}) decreases abruptly above x > 0.20 for NBT-ST, whereas the decrease is rather shallow for NBT-KBT and NBT-BT. The relatively small decrease in d_{33} in the latter two cases is because of the system's ability to retain its robust ferroelectric character by the field-stabilized long-range *P4mm* distortion Fig. S4 [81]. In the absence of this distortion in NBT-ST, the system increasingly loses its ferroelectric character, causing sharp decline in d_{33}. The composition dependence of d_{33} of NBT-ST is analogous to what have been reported for the Pb-based non-MPB systems $PbTiO_3$-$Bi(Ni_{0.5}Zr_{0.5})TiO_3$ and $PbTiO_3$-$Bi(Ni_{0.5}Hf_{0.5})TiO_3$ [83,84].

A comparison of the rhombohedral strain, defined as $\eta = 90 - \alpha_R$ (where α_R is the rhombohedral angle), of the three critical compositions in the poled state suggests that the rhombohedral strain is smallest ($\eta \sim 0.20°$) for NBT-ST. For NBT-BT ($\eta \sim 0.30°$) and NBT-KBT ($\eta \sim 0.29°$) η is
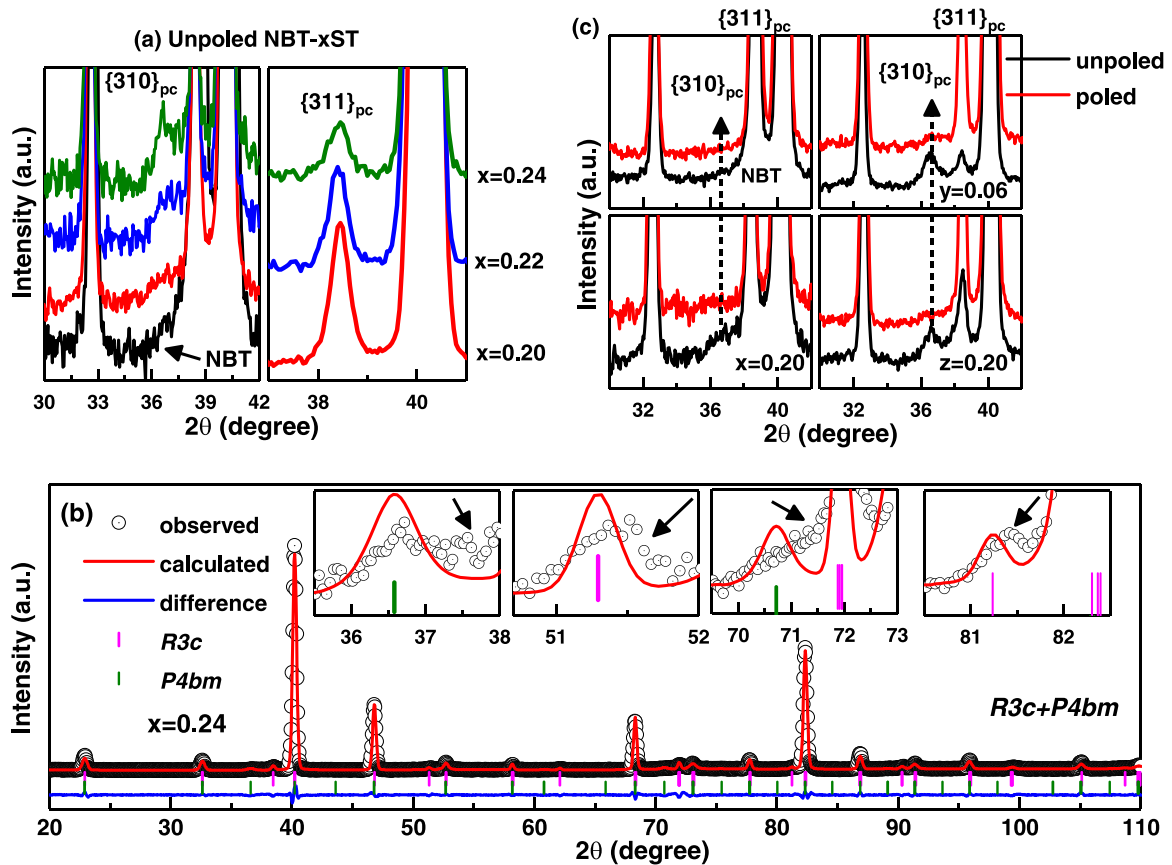
FIG. 4. (a) Evolution of the superlattice peaks corresponding to in-phase tilt $0.5\{310\}_{pc}$ and antiphase tilt $0.5\{311\}_{pc}$ in the neutron powder-diffraction (NPD) patterns of unpoled NBT-xST. (b) The NPD pattern of x = 0.24 fitted *R3c + P4bm* structure model at 30 °C. The arrows indicate misfit regions around the superlattice peaks. (c) Comparison of unpoled and poled NPD patterns of NBT, x = 0.20, y = 0.06, and z = 0.20.

comparatively large, Fig. S7b, Table S1 [81]. This is consistent with the fact that the remanent/maximum polarization of x = 0.20 is relatively small (P_r = 23 μC/cm^2) than that of y = 0.06 (P_r = 43.2 μC/cm^2) and z = 0.20 (P_r = 41.5 μC/cm^2), Fig. 1(b), Table S1 [81]. The smaller rhombohedral strain in NBT-ST makes domain switching easy as compared to the other two systems. This is also consistent with the smaller coercive field (E_c) of NBT-ST (x = 0.20), Fig. S7c, Table S1 [81]. Despite the lower rhombohedral lattice strain, the relatively large electrostrain of NBT-ST (unipolar electrostrain ~0.16%, and bipolar electrostrain ~0.18%) as compared to that of NBT-BT (unipolar electrostrain ~0.12%, and bipolar electrostrain ~0.14%) and NBT-KBT (unipolar electrostrain ~0.11% and bipolar electrostrain ~0.14%) can be attributed to NBT-ST exhibiting relatively large reverse switching of the rhombohedral ferroelastic domains, Figs. 1(c) and 1(d).

From the above, it is evident that the similarity of d_{33} of the critical compositions of NBT-BT, NBT-KBT and NBT-ST is not to be associated with a *R3c-P4mm* type interferroelectric instability. The next question is, *is there another factor which is common to all the three systems that primarily influences their d_{33}?* We investigated this aspect using NPD as it offers the benefit of detecting very weak octahedral tilt distortions, not possible to identify with the x-ray diffraction technique. Figure 4(a) shows the composition evolution of the NPD patterns of unpoled NBT-ST. For the sake of clarity, only limited

2θ regions are shown to highlight the superlattice peaks corresponding to the in-phase octahedral tilt (pseudocubic indices of the type $0.5\{ooe\}_{pc}$ where *o* and *e* represent odd and even integers, respectively) and antiphase tilt (pseudocubic indices $0.5\{ooo\}_{pc}$). A weak superlattice peak near the anticipated 2θ position of the $0.5\{310\}_{pc}$ becomes perceptible for x = 0.20 [Fig. 4(a)]. The intensity of this superlattice reflection grows with increasing concentration of ST. Concomitantly, the intensity of the $0.5\{311\}_{pc}$ superlattice peak corresponding to the *R3c* phase decreases dramatically. A similar composition evolution of two types of superlattice peaks has been reported for NBT-yBT [85] and NBT-zKBT [44]. Although there is a general tendency to associate the superlattice peaks corresponding to the in-phase tilt to the *P4bm* phase [85,86], our Rietveld analysis with the *R3c + P4bm* phase coexistence model revealed that this model is not sufficient to account for all the details of the NPD pattern as highlighted by the misfit regions in Fig. 4(b). A similar failure of this two-phase model has been reported earlier for NBT-yBT and NBT-zKBT [85,55], Fig. S8 [81]. It is important to note that this mismatch is not merely because the widths of the superlattice peaks are broader than those of the fundamental peaks. A close inspection rather reveals asymmetrical shape of the superlattice peak profiles, suggesting superposition of multiple closely spaced peaks. This is most likely due to one-dimensional (1D) projection of the complex 3D diffuse intensity patterns
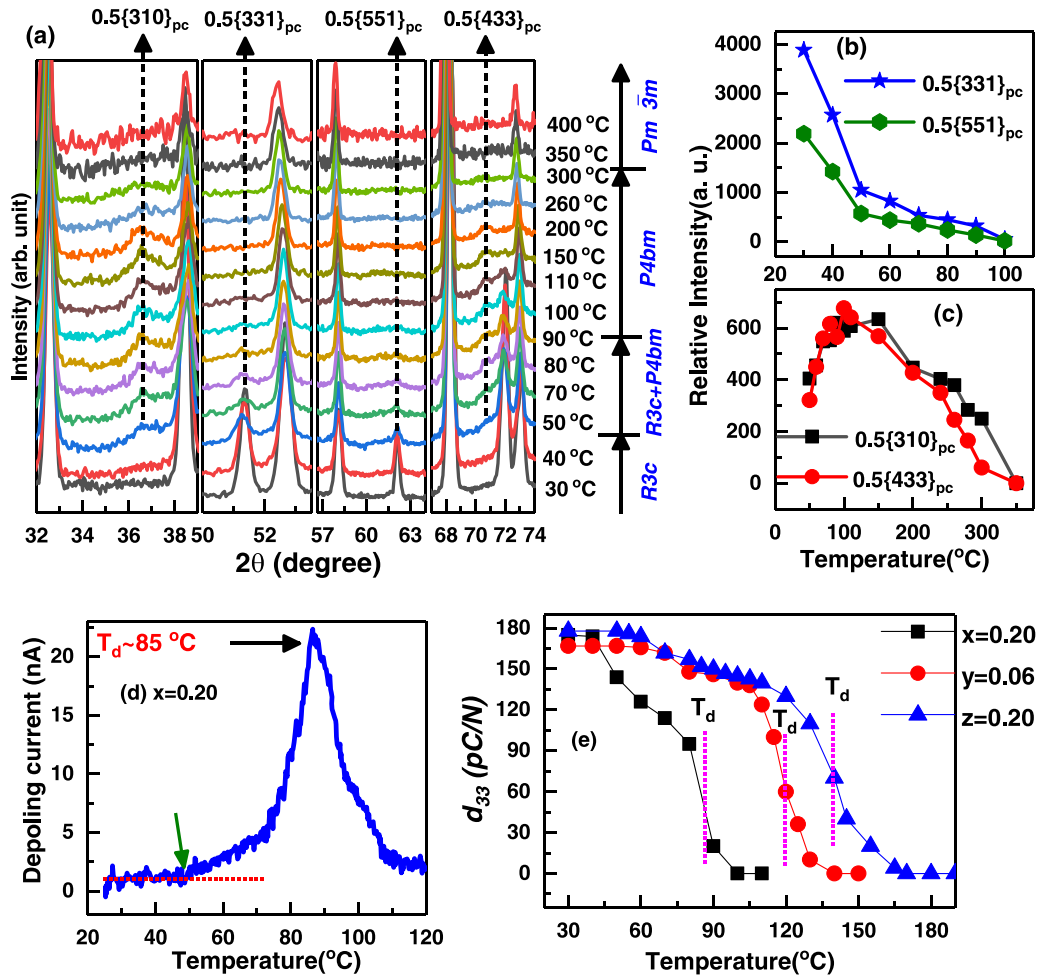
FIG. 5. (a) Evolution of NPD patterns of poled NBT-0.20ST sample with temperature. (b) Variation of the intensity of $0.5\{331\}_{pc}$ and $0.5\{551\}_{pc}$ superlattice reflections with temperature. (c) Variation of the intensity of $\{310\}_{pc}$ and $\{334\}_{pc}$ superlattice reflections with temperature. (d) Temperature dependence of the depoling current of x = 0.20. The sharp peak at $T_d \sim 85\,°C$ in (d) characterizes the depolarization temperature. (e) Variation of d_{33} as a function of annealing temperature of poled x = 0.20, y = 0.06 and z = 0.20. The depolarization temperatures (as obtained from the peak in the temperature dependent thermal depoling current measurements) are shown with dashed vertical lines in (e).

in the NPD pattern. Accordingly, we term this phase as the *disordered P4bm* phase. For the sake of a clear distinction, we may emphasize that *P4bm* model can successfully account for all the ½$\{ooe\}_{pc}$ type superlattice reflections in the NPD patterns of the parent compound NBT above 150 °C [82,85,86]. For such situations we refer to the *P4bm* phase as "ordered-*P4bm*". The ordered *P4bm* phase is found below the critical compositions of these three systems. Above their respective critical composition, the systems a exhibit disordered *P4bm* phase.

The $0.5\{310\}_{pc}$ superlattice reflection corresponding to disordered *P4bm* phase disappears after poling the critical compositions of all the three systems NBT-ST (x = 0.20), NBT-yBT (y = 0.06), and NBT-zKBT (z = 0.20), Fig. 4(c). Consistent with the XRD results, the NPD patterns of poled specimens of the critical compositions, the three systems could be satisfactorily fit with *R3c* structural model, Fig. S9a–c [81]. We followed the structural description of Megaw and Darlington [87] to describe the rhombohedral (*R3c*) phase as it offers direct estimation of the polar cation dis-

placement (s), octahedral strain, and octahedral tilt angle. It is important to note that antiphase octahedral tilt angle of NBT-ST: x = 0.20 is considerably smaller ($\sim 6.6°$) as compared to that of NBT-BT:y = 0.06($\sim 7.1°$) and NBT-KBT: z = 0.20($\sim 7.06°$), Table S1 [81]. A concomitant smaller off-centered displacements of A-site and Ti atoms in NBT-ST: x = 0.20 in comparison to NBT-BT:y = 0.06 and NBT-KBT: z = 0.20 (see Table S1), clearly suggests the coupled nature of the antiphase octahedral tilt and polar cationic displacements in the three systems.

For a better appreciation of how the disordered *P4bm* phase gets stabilized in the system, we performed a high temperature NPD study of poled specimens during the heating cycle. The $0.5\{ooe\}_{pc}$ type superlattice reflections becomes discernible at 50 °C [Fig. 5(a)]. This is accompanied by a concomitant decrease in the intensity of the $0.5\{ooo\}_{pc}$ superlattice peaks, Fig. 5(b). The intensity of the $0.5\{ooe\}_{pc}$ superlattice peaks becomes maximum at ~ 100 °C and decreases thereafter on further heating, Fig. 5(c). The superlattice reflections corresponding to antiphase and in-phase octahedral tilts are visible
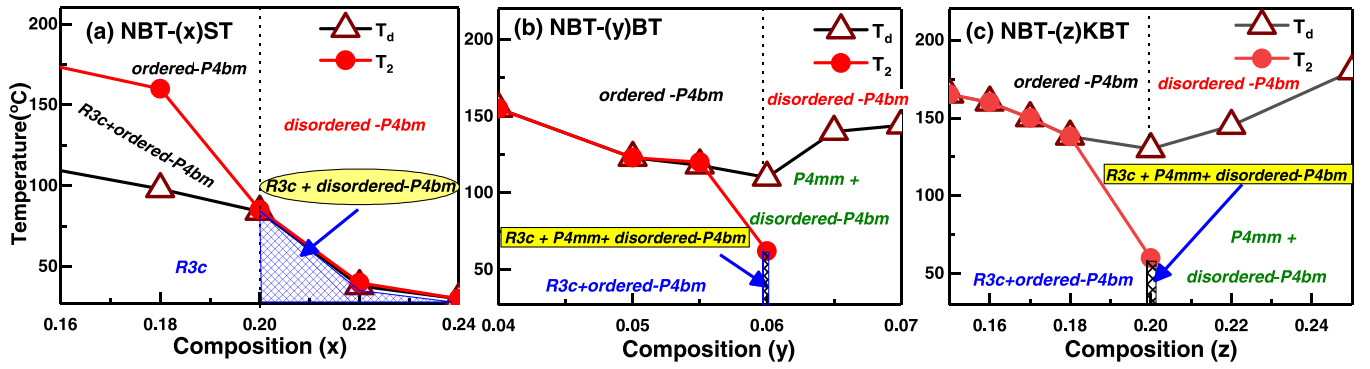
FIG. 6. Phase diagrams of unpoled (a) NBT-(x)ST, (b) NBT-(y)BT, and (c) NBT-(Z)KBT. $T_d \rightarrow$ depolarization temperature; $T_2 \rightarrow R3c - P4bm$ phase transition temperature.

in the temperature range 50 °C–90 °C. Important to note that 90 °C happens to be the temperature above which the residue of the poling induced $R3c$ phase vanishes completely. This temperature also coincides with the peak in the thermal depoling current [Fig. 5(d)]. The onset of thermal depoling, however, starts earlier at ∼ 50 °C which matches with the temperature corresponding to the onset of the in-phase octahedral tilt, Fig. 5(a). A distinct signature of this phenomenon is also evident in the small yet distinct decrease in d_{33} above 50 °C, Fig. 5(e). Thermal depoling of y = 0.06 and z = 0.20 starts at ∼55 °C and is associated with a simultaneous occurrence of the in-phase octahedral tilt (disordered $P4bm$ phase) and ferroelectric $P4mm$ phase, Fig. 5(e). The depolarization temperature (T_d), as determined from the peak in the temperature dependent thermal depoling current measurements, is related to the complete vanishing of poling induced $R3c$ phase. For y = 0.06 and z = 0.20 it correspond to a complete disappearance of the $P4mm$ phase [42]. We attempted to fit the NPD pattern at 150 °C using the $P4bm$ structural model. The large misfit between the observed and the calculated profiles of the superlattice peaks (Fig. S10b [81]) suggests the inadequateness of this structural model. As stated earlier, this phase is referred to as the disordered $P4bm$ phase.

Based on the temperature dependent x-ray and neutron powder diffraction studies of NBT-ST, NBT-BT, and NBT-KBT systems, we show a comparison of the phase diagrams of three systems in the proximity of their respective critical compositions Figs. 6(a)–6(c). We used neutron diffraction study not only to determine the temperature corresponding to the onset of the $P4bm$ distortion (ascertained from the onset of the 0.5{ooe}$_{pc}$ superlattice peaks during heating), but also to ascertain about its nature (order/disordered $P4bm$ phase). From the temperature dependent XRD measurements we determined the temperatures corresponding to the disappearance of the long-range ferroelectric ($R3c$/$P4mm$) order in these systems. It is evident from these phase diagrams that on cooling, the $R3c$ rhombohedral distortion in $x \geqslant 0.20$ (NBT-ST system) is forced to develop within the *disordered*

$P4bm$ matrix. This region is represented as $R3c$ + disordered-$P4bm$ in the phase diagram, Fig. 6(a). For NBT-BT [Fig. 6(b)] and NBT-KBT [Fig. 6(c)], on the other hand, the system develops $P4mm$ ferroelectric distortion within the disordered $P4bm$ matrix [Figs. 6(b) and 6(c)]. There is a very narrow region adjacent to the critical composition wherein NBT-BT and NBT-KBT exhibit $P4mm + disordered - P4bm + R3c$ phases, Figs. 6(b) and 6(c).

IV. CONCLUSIONS

In summary, our systematic investigation of the three NBT-based systems NBT-ST, NBT-BT, and NBT-KBT revealed that despite the similarity of the structures (cubiclike) of their critical compositions on the global scale, they exhibit distinctly different structures on the local scale. Using Eu^{+3} PL as a spectroscopic tool, we demonstrate that the local structure of critical compositions of unpoled NBT-yBT (y = 0.06) and NBT-zKBT (z = 0.20) are comprised of the coexistence of $P4mm$ and $R3c$ phases. In contrast, the critical composition (x = 0.20) of unpoled NBT-ST exhibits only the $R3c$ phase on the local scale. We discovered that irrespective of whether the system exhibits $R3c$-$P4mm$ interferroelectric instability or not, the critical compositions showing similar maximum d_{33} correspond to the onset of a "disordered-$P4bm$" phase in all the three cases. This factor appears to overwhelm the $R3c$-$P4mm$ interferroelectric instability in both NBT-KBT and NBT-BT, making the piezoelectric response of their critical compositions similar to the critical composition of the NBT-ST system (which lacks the $R3c$-$P4mm$ instability).

[1] B. Jaffe, R. S. Roth, and S. Marzullo, J. Appl. Phys. **25**, 809 (1954).

[2] B. Jaffe, W. R. Cook, and H. Jaffe, *Piezoelectric Ceramics* (Academic, New York, 1971).

[3] J. Y. Li, R. C. Rogan, E. Ustundag, and K. Bhattacharya, Nat. Mater. **4**, 776 (2005).

[4] H. Fu and R. E. Cohen, Nature (London) **403**, 281 (2000).

[5] D. Damjanovic, J. Am. Ceram. Soc. **88**, 2663 (2005).

[6] D. Damjanovic and M. Demartin, J. Phys. D **29**, 2057 (1996).

[7] S. Li, W. Cao, and L. E. Cross, J. Appl. Phys. **69**, 7219 (1991).

[8] D. Damjanovic, Rep. Prog. Phys. **61**, 1267 (1998).

[9] E. U-Directive, 2002/95/EC: Restriction of the use of certain hazardous substances in electrical and electronic equipment (RoHS), Official Journal of the European Union 46, 19 (2003).

[10] Y. Saito, H. Takao, T. Tani, T. Nonoyama, K. Takatori, T. Homma, T. Nagaya, and M. Nakamura, Nature (London) **432**, 84 (2004).

[11] W. Liu and X. Ren, Phys. Rev. Lett. **103**, 257602 (2009).

[12] J. Rödel and J.-F. Li, MRS Bull. **43**, 576 (2018).

[13] J. Wu, J. Appl. Phys. **127**, 190901 (2020).

[14] T. Zheng, J. Wu, D. Xiao, and J. Zhu, Prog. Mater. Sci. **98**, 552 (2018).

[15] K. Brajesh, M. Abebe, and R. Ranjan, Phys. Rev. B **94**, 104108 (2016).

[16] M. Abebe, K. Brajesh, A. Mishra, A. Senyshyn, and R. Ranjan, Phys. Rev. B **96**, 014113 (2017).

[17] B. Wu, H. J. Wu, J. G. Wu, D. Q. Xiao, J. G. Zhu, and S. J. Pennycook, J. Am. Chem. Soc. **138**, 15459 (2016).

[18] X. P. Wang, J. G. Wu, D. Q. Xiao, J. G. Zhu, X. J. Cheng, T. Zheng, and X. J. Wang, J. Am. Chem. Soc. **136**, 2905 (2014).

[19] H. Tao, H. J. Wu, Y. Liu, Y. Zhang, J. G. Wu, F. Li, X. Lyu, C. L. Zhao, D. Q. Xiao, J. G. Zhu, and S. J. Pennycook, J. Am. Chem. Soc. **141**, 13987 (2019).

[20] K. Xu, J. Li, X. Lv, J. G. Wu, X. X. Zhang, D. Q. Xiao, and J. G. Zhu, Adv. Mater. **28**, 8519 (2016).

[21] B. N. Rao, R. Datta, S. S. Chandrashekaran, D. K. Mishra, V. Sathe, A. Senyshyn, and R. Ranjan, Phys. Rev. B **88**, 224103 (2013).

[22] S. Gorfman and P. A. Thomas, J. Appl. Crystallogr. **43**, 1409 (2010).

[23] S. Gorfman, A. M. Glazer, Y. Noguchi, M. Miyayama, H. Luo, and P. A. Thomas, J. Appl. Crystallogr. **45**, 444 (2012).

[24] E. Aksel, J. S. Forrester, J. L. Jones, P. A. Thomas, K. Page, and M. R. Suchomel, Appl. Phys. Lett. **98**, 152901 (2011).

[25] V. Dorcet and G. Trolliard, Acta Mater. **56**, 1753 (2008).

[26] C.-S. Tu, I. G. Siny, and V. H. Schmidt, Phys. Rev. B **49**, 11550 (1994).

[27] I. Levin and I. M. Reaney, Adv. Funct. Mater. **22**, 3445 (2012).

[28] J. Kreisel, A. M. Glazer, P. Bouvier, and G. Lucazeau, Phys. Rev. B **63**, 174106 (2001).

[29] V. A. Shuvaeva, D. Zekria, A. M. Glazer, Q. Jiang, S. M. Weber, P. Bhattacharya, and P. A. Thomas, Phys. Rev. B **71**, 174114 (2005).

[30] K. Datta, A. Richter, M. Gobbels, R. B. Neder, and B. Mihailova, Phys. Rev. B **90**, 064112 (2014).

[31] M. Matsuura, H. Iida, K. Hirota, K. Ohwada, Y. Noguchi, and M. Miyayama, Phys. Rev. B **87**, 064109 (2013).

[32] G. D. Adhikary, V. Dwij, A. Senyshyn, V. Sathe, and R. Ranjan, Phys. Rev. Mater. **5**, 064414 (2021).

[33] S. -T. Zhang, A. B. Kounga, E. Aulbach, H. Ehrenberg, and J. Rödel, Appl. Phys. Lett. **91**, 112906 (2007).

[34] X. Liu and X. Tan, Adv. Mater. **28**, 574 (2016).

[35] W. Jo, R. Dittmer, M. Acosta, J. Zang, C. Groh, E. Sapper, K. Wang, and J. Rödel, J. Electroceram. **29**, 71 (2012).

[36] T.-M. Usher, I. Levin, J. E. Daniels, and J. L. Jones, Sci. Rep. **5**, 14678 (2015).

[37] B. N. Rao, L. Olivi, V. Sathe, and R. Ranjan, Phys. Rev. B **93**, 024106 (2016).

[38] G. O. Jones and P. A. Thomas, Acta Crystallogr. Sec. B **58**, 168 (2002).

[39] S. B. Vakhrushev, B. E. Kvyatkovskii, R. S. Malysheva, N. M. Okuneva, and P. P. Syrnikov, Sov. Phys. Solid State **27**, 455 (1985).

[40] G. A. Smolenskii, V. A. Isupv, A. I. Afranovskaya, and N. N. Kainik, J. Solid State Phys. **11**, 2651 (1961).

[41] B. N. Rao and R. Ranjan, Phys. Rev. B **86**, 134103 (2012).

[42] G. D. Adhikary, B. Mahale, A. Senyshyn, and R. Ranjan, Phys. Rev. B **102**, 184113 (2020).

[43] G. D. Adhikary and R. Ranjan, J. Appl. Phys. **128**, 204102 (2020).

[44] G. D. Adhikary, D. K. Khatua, A. Senyshyn, and R. Ranjan, Phys. Rev. B **99**, 174112 (2019).

[45] P. G. Groszewicz, M. Gröting, H. Breitzke, W. Jo, K. Albe, G. Buntkowsky, and J. Rödel, Sci. Rep. **6**, 31739 (2016).

[46] B. N. Rao, M. Avdeev, B. Kennedy, and R. Ranjan, Phys. Rev. B **92**, 214107 (2015).

[47] S. P. Singh, R. Ranjan, A. Senyshyn, D. Trots, and H. Boysen, J. Phys.: Condens. Matter **21**, 375902 (2009).

[48] O. Elkechai, P. Marchel, P. Thomas, M. Manier, and J. P. Mercurio, J. Mater. Chem. **7**, 91 (1997).

[49] F. Cordero, F. Craciun, F. Trequattrini, E. Mercadelli, and C. Galassi, Phys. Rev. B **81**, 144124 (2010).

[50] Y. Hiruma, K. Yoshii, H. Nagata, and T. Takenaka, Ferroelectrics **346**, 114 (2007).

[51] I. Levin, I. M. Reaney, E.-M. Anton, W. Jo, J. Rödel, J. Pokorny, L. A. Schmitt, H.-J. Kleebe, M. Hinterstein, and J. L. Jones, Phys. Rev. B **87**, 024113 (2013).

[52] R. Garg, B. N. Rao, A. Senyshyn, P. S. R. Krishna, and R. Ranjan, Phys. Rev. B **88**, 014103 (2013).

[53] C. Ma, H. Guo, S. P. Beckman, and X. Tan, Phys. Rev. Lett. **109**, 107602 (2012).

[54] K. Datta, R. B. Neder, A. Richter, M. Gobbels, J. C. Neuefeind, and B. Mihailova, Phys. Rev. B **97**, 184101 (2018).

[55] G. D. Adhikary, D. K. Khatua, A. Senyshyn, and R. Ranjan, Acta Mater. **164**, 749 (2019).

[56] M. Otonicar, S. D. Škapin, M. Spreitzer, and D. Suvorov, J. Eur. Ceram. Soc. **30**, 971 (2010).

[57] H. Luo, H. Liu, S. Deng, S. Hu, L. Wang, B. Gao, S. Sun, Y. Ren, L. Qiao, and J. Chen, Acta Mater. **208**, 116711 (2021).

[58] X. Liu, S. Xue, F. Wang, J. Zhai, and B. Shen, Acta Mater. **164**, 12 (2018).

[59] H. He, X. Lu, M. Li, Y. Wang, Z. Li, Z. Lu, and L. Lu, J. Mater. Chem. C **8**, 2411 (2020).

[60] D. Rout, K. S. Moon, S. J. L. Kang, and I. W. Kim, J. Appl. Phys. **108**, 084102 (2010).

[61] S. Kim, H. Choi, S. Han, J. S. Park, M. H. Lee, T. K. Song, M. H. Kim, D. Do, and W. J. Kim, J. Eur. Ceram. Soc. **37**, 1379 (2017).

[62] H. Unoki and T. Sakudo, J. Phys. Soc. Jpn. **23**, 546 (1967).

[63] K. A. Müller and H. Burkard, Phys. Rev. B **19**, 3593 (1979).

[64] R. Ranjan and A. Dviwedi, Solid State Commun. **135**, 394 (2005).

[65] J. E. Daniels, W. Jo, J. Rödel, and J. L. Jones, Appl. Phys. Lett. **95**, 032904 (2009).

[66] B. Wylie-van Eerd, D. Damjanovic, N. Klein, N. Setter, and J. Trodahl, Phys. Rev. B **82**, 104112 (2010).

[67] P. B. Groszewicz, H. Breitzke, R. Dittmer, E. Sapper, W. Jo, G. Buntkowsky, and J. Rodel, Phys. Rev. B **90**, 220104(R) (2014).

[68] N. H. Khansur, M. Hinterstein, Z. Wang, C. Groh, W. Jo, and J. E. Daniels, Appl. Phys. Lett. **107**, 242902 (2015).

[69] M. Hoelzel, A. Senyshyn, R. Gilles, H. Boysen, and H. Fuess, Neutron News **18**, 23 (2007).

[70] J. Rodrigues-Carvajal, *2000 FULLPROF. A Rietveld Refinement and Pattern Matching Analysis Program* (Laboratoire Leon Brillouin (CEACNRS), France, 2000).

[71] J. C. G. Bünzli, Coord. Chem. Rev. **293–294**, 19 (2015).

[72] K. Binnemans, Coord. Chem. Rev. **295**, 1 (2015).

[73] K. Jorgensen and B. R. Judd, Mol. Phys. **8**, 281 (1964).

[74] D. K. Khatua, A. Kalaskar, and R. Ranjan, Phys. Rev. Lett. **116**, 117601 (2016).

[75] A. De and R. Ranjan, Mater. Horiz. **7**, 1101 (2020).

[76] J. Hao, Y. Zhang, and X. Wei, Angew. Chem. Int. Ed. **50**, 6876 (2011).

[77] S. A. Lourenco, N. O. Dantas, E. O. Serqueira, W. E. F. Ayta, A. A. Andrade, M. C. Filadelpho, J. A. Sampaio, M. J. V. Bell, and M. A. Pereira-Da-Silva, J. Lumin. **131**, 850 (2011).

[78] D. K. Khatua, A. Agarwal, N. Kumar, and R. Ranjan, Acta Mater. **145**, 429 (2018).

[79] A. De and R. Ranjan, Phys. Rev. B **98**, 094111 (2018).

[80] A. De and R. Ranjan, J. Appl. Phys. **128**, 124104 (2020).

[81] See Supplemental Material at http://link.aps.org/supplemental/10.1103/PhysRevB.104.184102 for the information on Rietveld refinements of room temperature NPD and XRPD patterns, Raman Spectroscopy, and other details.

[82] G. D. Adhikary, B. Mahale, B. N. Rao, A. Senyshyn, and R. Ranjan, Phys. Rev. B **103**, 184106 (2021).

[83] R. Pandey, B. Narayan, D. K. Khatua, S. Tyagi, A. Mostaed, M. Abebe, V. Sathe, I. M. Reaney, and R. Ranjan, Phys. Rev. B **97**, 224109 (2018).

[84] U. Shankar, N. Kumar, B. Narayan, D. Swain, A. Senyshyn, and R. Ranjan, Phys. Rev. B **100**, 094101 (2019).

[85] G. D. Adhikary, D. K. Khatua, A. Mishra, A. De, N. Kumar, S. Saha, U. Shankar, A. Senyshyn, B. N. Rao, and R. Ranjan, Phys. Rev. B **100**, 134111 (2019).

[86] G. O. Jones and P. A. Thomas, Acta Crystallogr. Sec. B **56**, 426 (2000).

[87] H. D. Megaw and C. N. W. Darlington, Acta Crystallogr. Sec. A **31**, 161 (1975).